

UNCLASSIFIED

Defense Technical Information Center
Compilation Part Notice

ADP014170

TITLE: Using High-Fidelity Analysis Methods and Experimental Results to Account for the Effects of Imperfections on the Buckling Response of Composite Shell Structures

DISTRIBUTION: Approved for public release, distribution unlimited
Availability: Hard copy only.

This paper is part of the following report:

TITLE: Reduction of Military Vehicle Acquisition Time and Cost through Advanced Modelling and Virtual Simulation [La reduction des couts et des delais d'acquisition des vehicules militaires par la modelisation avancee et la simulation de produit virtuel]

To order the complete compilation report, use: ADA415759

The component part is provided here to allow users access to individually authored sections of proceedings, annals, symposia, etc. However, the component should be considered within the context of the overall compilation report and not as a stand-alone technical report.

The following component part numbers comprise the compilation report:

ADP014142 thru ADP014198

UNCLASSIFIED

Using High-Fidelity Analysis Methods and Experimental Results to Account for the Effects of Imperfections on the Buckling Response of Composite Shell Structures

James H. Starnes, Jr. and Mark W. Hilburger
NASA Langley Research Center
Hampton, VA 23681-2199, USA

ABSTRACT

The results of an experimental and analytical study of the effects of initial imperfections on the buckling response of unstiffened thin-walled compression-loaded graphite-epoxy cylindrical shells are presented. The analytical results include the effects of traditional and nontraditional initial imperfections and uncertainties in the values of selected shell parameters on the buckling loads of the shells. The nonlinear structural analysis results correlate very well with the experimental results. The high-fidelity nonlinear analysis procedure used to generate the analytical results can also be used to form the basis of a new shell design procedure that could reduce the traditional dependence on empirical results in the shell design process.

KEYWORDS: high-fidelity nonlinear structural analysis, composite shells, shell stability, initial imperfections

INTRODUCTION

With the increasing need to produce lighter-weight aerospace structures, advanced composite materials are being used in new structural designs to reduce structural weight. One of the contributors to the high cost of developing new designs for aerospace structures made of composite materials is the cost of developing material properties and structural design allowable values. To reduce this cost, improved design methods appropriate for advanced composite materials are needed. The present paper describes a verified high-fidelity nonlinear structural analysis procedure that has the potential for reducing the traditional dependence on empirical results in the structural design process for composite structures. Reducing the traditional dependence on empirical results in the design process means that the more than ten thousand structural-design-allowable-value tests that are commonly conducted today could be reduced to, say, several hundred carefully selected tests needed to verify the design at various dimensional levels (e.g., coupons, structural details, panels, etc.). A reduction in the number of tests needed to support the current empirically based structural design process should reduce some of the costs associated with developing a new structural design.

Today, designers often use a design-level analysis procedure with empirical data to develop new structural designs for strength and buckling critical structures. The traditional approach to designing thin-walled buckling-resistant isotropic shell structures is to predict the buckling load of the shell with a deterministic linear bifurcation buckling analysis that is usually based on nominal structural dimensions and material properties of an idealized, geometrically perfect shell. The results of this analysis are then reduced by an empirical “knockdown” factor (e.g., Ref. 1) to account for the difference between the predicted buckling load and the actual buckling load of the shell determined from tests. The knockdown factor used in the design of buckling-resistant shells is often based on the

“Lower Bound” design recommendations reported in such sources as Reference 1. This design philosophy can potentially result in overly conservative designs for these structures. While it is generally recognized that initial geometric shell-wall imperfections are a major contributor to the discrepancy between predicted and experimentally measured shell buckling loads (e.g., Ref. 2), the traditional sources of design knockdown factors do not include data or information related to the sensitivity of the buckling loads to initial imperfections, or information for composite shell structures. Recent studies (e.g., Refs. 3-4) have shown that traditional geometric shell-wall imperfections, and other nontraditional forms of imperfections or variations in geometric and material parameters, loading conditions, and boundary conditions can significantly affect the buckling load of compression-loaded composite shell structures. The effects of these traditional and nontraditional classes of initial imperfections on composite shell buckling are generally not well understood by structural designers. Modern high-fidelity nonlinear analysis procedures (e.g., Ref. 5) offer the opportunity to improve some of the engineering approximations that are used in the shell design process, and to provide insight into the effects of traditional and nontraditional imperfections on the buckling response of composite shell structures.

The present paper describes a high-fidelity nonlinear structural analysis procedure that can be used for the design of buckling-resistant composite shell structures. The results of an experimental and analytical study of the effects of initial imperfections on the buckling response of graphite-epoxy cylindrical shells are presented. The results identify the effects of traditional initial geometric shell-wall imperfections and several relatively unknown and nontraditional imperfections, such as shell-end geometric imperfections, shell-wall thickness variations, variations in loads applied to the ends of the shells, and variations in the boundary conditions, on the buckling loads of these shells. The effects of manufacturing anomalies caused by small gaps between adjacent pieces of graphite-epoxy tape in a shell-wall layer or ply of graphite-epoxy material are also discussed. The high-fidelity nonlinear shell analysis procedure accurately accounts for the effects of these traditional and nontraditional imperfections on the shell buckling loads. The analysis results are compared with the experimental results, and this comparison suggests that the analysis procedure can be used for determining accurate, high-fidelity design knockdown factors for predicting shell buckling loads in the design process. This analysis procedure can be used to form the basis for a shell design approach that should make it possible to reduce the need for empirical knockdown factors currently used in design, and to reduce the cost of developing buckling-resistant shell designs. Once this high-fidelity analysis-based design procedure is established for buckling-critical composite shell structures, it could be generalized to form the basis of an analysis-based design procedure for other composite structural design applications.

TEST SPECIMENS, IMPERFECTION MEASUREMENTS, AND TESTS

Test Specimens

The specimens tested in this study were fabricated from 12-in.-wide, 0.005-in.-thick AS4/3502 graphite-epoxy prepreg unidirectional tape material made by Hercules, Inc. The nominal unidirectional lamina properties of a typical 0.005-in.-thick ply with a fiber volume fraction of 0.62 are: longitudinal compression modulus $E_1 = 18.5$ Msi, transverse modulus $E_2 = 1.64$ Msi, in-plane shear modulus $G_{12} = 0.87$ Msi, and major Poisson's ratio $\nu_{12} = 0.30$. The material was laid up on a 15.75-in.-diameter mandrel and cured in an autoclave to form six shells with different shell-wall laminates. These shells include 8- and 16-ply shells with either $[45/0_2]_s$, $[45/90_2]_s$, $[45/0/90]_s$, $[45/0_2]_{2s}$, $[45/90_2]_{2s}$, or $[45/0/90]_{2s}$ laminates. The resulting shells are referred to herein as shells or specimens C1 through C6, respectively. These specimens had a nominal length of 16.0 in. and a nominal radius of 8.0 in. The 8- and 16-ply specimens had nominal shell-wall thicknesses of 0.04 in. and 0.08 in., and shell-radius-to-thickness

ratios of 200 and 100, respectively. Both ends of the specimens were potted in an aluminum-filled epoxy material to prevent the ends of the specimens from failing prematurely. The potting material extended approximately 1.0 inch along the length of the specimens at each end resulting in an exposed length that was approximately 14.0 in. long. The ends of the specimens were machined flat and parallel to facilitate proper load introduction during the tests. A photograph of a typical specimen and the specimen coordinate system used to represent the corresponding geometry is shown in Fig.1. The shell length, test-section length, radius, and thickness are designated as L , L_T , R and t , respectively.

Imperfection Measurements

Three-dimensional surveys of the inner and outer shell-wall surfaces of the specimens were made prior to testing the specimens to determine their initial geometric shell-wall imperfection shapes and shell-wall thickness distributions. Measurements were taken over a uniform grid with increments of 0.125 in. in the axial direction and 0.139 in. (approximately 1° of arc) in the circumferential direction over the exposed surfaces of the specimens. The inner surface measurement was used to determine the initial geometric shell-wall imperfection shape of a specimen, and the difference between the outer and inner surface measurements was used to determine the shell-wall thickness distribution. A contour plot of the nondimensionalized initial geometric shell-wall mid-surface imperfections for specimen C3 is shown in Fig. 2. The measured shell-wall imperfection w_o is nondimensionalized by the average measured shell-wall thickness $t_{ave} = 0.0381$ inches. These results indicate that the initial geometric shell-wall imperfection is periodic in the circumferential direction and has slight variations in the axial direction. The amplitude of the imperfection varies from $+1.341t_{ave}$ to $-1.535t_{ave}$. A contour plot of the nondimensionalized shell-wall thickness variation for specimen C3 is shown in Fig. 3, where the measured thickness values t_o are nondimensionalized by the average measured shell-wall thickness t_{ave} . These results indicate that the shell-wall thickness, and hence the laminate stiffnesses, varies significantly over a short distance. The thickness varies from 0.928 to $1.321t_{ave}$. Most of the thickness variation is due to local variations in the resin content of the laminate associated with the fabrication process. However, the darker angular pattern in Fig. 3 is due to small gaps between adjacent pieces of graphite-epoxy tape in some of the laminate plies that were generated during the lay-up and curing processes. Such a region is referred to herein as a lamina ply-gap or a ply-gap. These locally thin shell-wall regions have a significant shell-wall mid-surface eccentricity, and have reduced stiffnesses relative to the rest of the shell wall. Lamina ply-gaps with gap widths as large as 0.15 in. have been observed in some of the specimens. The lighter angular patterns in Fig. 3 are caused by locally thickened regions of the outermost plies of the laminate that develop during the curing process to form outer shell-wall surface ridges. Typical magnified cross-sectional views illustrating the microstructure of typical ply-gaps and outer surface ridges in a laminated shell wall are presented in Ref. 3.

Measurements of the specimen top and bottom loading surfaces were made every degree around the circumference of the specimens to determine the variation in the shell-end or loading-surface geometry. Typical top and bottom shell-end geometry variations are shown in Fig. 4 for specimen C3 and are denoted by $\delta_{top}(\theta)$ and $\delta_{bot}(\theta)$, respectively. The maximum amplitude of this shell-end variation is approximately 0.0015 in., or approximately 0.01% of the specimen length.

Test Apparatus and Tests

The specimens were instrumented with electrical resistance strain gages, and direct-current differential transducers (DCDT's) were used to measure displacements. Three non-collinear DCDT's were positioned at three corners of the upper loading platen

of the test machine and used to measure the end-shortening displacement Δ and the rotations ϕ_y and ϕ_z of the loading platen as illustrated in Fig. 1. The specimens were loaded in compression with a 300,000-lb hydraulic universal-testing machine by applying an end-shortening displacement to the shell ends. The upper loading platen was aligned with the loading surface of the specimen as well as possible before the test by adjusting leveling bolts in the corners of the upper loading platen until strains measured by selected strain gages indicated a uniform axial strain distribution in the shell wall. The shadow moiré interferometry technique was used to observe the shell-wall radial (perpendicular to the shell outer surface) deformation patterns. All data were recorded with a data acquisition system, and the moiré patterns were recorded photographically and on videotape. The specimens were loaded until buckling or failure of the shells occurred.

FINITE-ELEMENT MODELS AND ANALYSES

Nonlinear Analysis Procedure

The shells considered in this study were analyzed with the STAGS (STructural Analysis of General Shells) nonlinear shell analysis code.⁵ STAGS is a finite-element code developed for the nonlinear static and dynamic analysis of general shells, and includes the effects of geometric and material nonlinearities in the analysis. The code uses both the modified and full Newton methods for its nonlinear solution algorithms, and accounts for large rotations in a shell by using a co-rotational algorithm at the element level. A pseudo arc-length path-following method is used to continue a solution past the limit points of a nonlinear response. The transient analysis option in STAGS uses proportional structural damping and an implicit numerical time-integration method.

The responses of the shells were determined using the following analysis procedure. The prebuckling responses were determined using the geometrically nonlinear quasi-static analysis capability in STAGS. The pseudo arc-length path-following method was used to compute the initial shell response until just before buckling occurred. The unstable buckling response of the shell was predicted using the nonlinear transient analysis option of the code. The transient analysis was initiated from an unstable equilibrium state close to the limit point by incrementing the end displacement by a small amount. The transient analysis was continued until the kinetic energy in the shell had dissipated, which indicated that the transient response had attenuated. Once the transient analysis had attenuated to a near-steady-state solution, the load relaxation option of the code was used to establish a static equilibrium state. Conventional linear bifurcation buckling analysis results were also determined with STAGS for comparison with the nonlinear response results.

Finite-Element Models

A typical finite-element model of a specimen is illustrated in Fig. 1. The STAGS 410 quadrilateral element was used in the models. The elements of the finite-element mesh are approximately 0.2-in. by 0.2-in. square. Each element has four integration points, which are distributed in such a way as to provide a modeling resolution of approximately 0.1-in. by 0.1-in. square. This integration-point spacing is on the order of the measurement-point spacing used when measuring the initial geometric imperfections of the specimens. This highly refined mesh is necessary to model rapidly varying geometric and material parameters such as nonuniform shell-wall thicknesses and lamina stiffness properties.

Geometrically perfect and imperfect shells were analyzed in the present study. Nominal shell geometry, laminate thickness, lamina mechanical properties, and boundary conditions were used to model the geometrically perfect shells. The nominal boundary conditions consist of setting the circumferential and normal displacements v and w

equal to zero in the 1.0-in.-long potted boundary illustrated in Fig. 1, setting $u(L/2, \theta) = 0$, and applying a uniform end-shortening $u(-L/2, \theta) = \Delta$. The geometrically perfect finite-element models were modified to include the effects of the measured shell imperfections in order to model the geometrically imperfect shells. These modeling modifications include the effects of the measured initial geometric shell-wall imperfections, shell-wall thickness variations, local shell-wall lamina ply-gaps, thickness-adjusted lamina properties, boundary stiffness conditions, shell-end geometric imperfections, and nonuniform end loads.

The initial geometric shell-wall imperfection $w_o(x, \theta)$ is included in the finite-element models by introducing an initial normal perturbation to each node of the mesh by using a user-written subroutine with STAGS for that purpose. A linear interpolation algorithm was used to calculate the value of the imperfection for the coordinates of each finite-element node based on the measured shell-wall data. The shell-wall thickness, mid-surface eccentricity, and lamina material properties are adjusted at each integration point of each element in the finite-element models. The shell-wall eccentricity is calculated relative to the average shell-wall mid-surface. The lamina properties are adjusted by using the rule of mixtures. In the rule-of-mixtures calculations, it is assumed that any variation in the lamina ply thickness from the nominal thickness is due to a variation in resin volume only, and that the fiber volume remains constant for each ply. Details of modeling the ply-gap regions and results from a numerical parametric study of the effects of ply gaps on the buckling loads of these composite shells are given in Ref. 3.

To provide a better simulation of the elastic boundary constraints provided by the potting material at the ends of the specimens, effective axial and radial potting-support stiffnesses were determined for each shell specimen using a two-dimensional generalized plane-strain finite-element analysis of the potting-material-shell-wall detail. The predicted results indicate that the effective axial potted-shell stiffness range from 1.1 to 2.4 times the nominal shell-wall stiffness and the nominal effective radial potting-support stiffness was predicted to be approximately equal to $1.0E5$ lbf/in. In the present study the nominal effective axial potted-shell stiffnesses are equal to 1.2, 2.0, 1.3, 1.1, 1.4, and 1.2 times the nominal shell-wall stiffness of shells C1 through C6, respectively. The predicted results also indicate that the increase in the effective axial potted-shell stiffness is inversely proportional to the nominal shell wall stiffness. Details on the boundary stiffness analyses and effects of the boundary stiffness on the response of the shells are given in Refs. 3-4.

Nonuniform specimen end loading is due to initial specimen-end or loading-surface imperfections and to upper loading-platen rotations that are measured during the experiment. First, the measured upper and lower specimen-end imperfections $\delta_{top}(\theta)$ and $\delta_{bot}(\theta)$ were included in the finite-element model by introducing an initial in-plane axial perturbation to the nodes at the loaded ends of the shell. Then, the compression load was applied to the shell in two parts. The nonuniform specimen-end imperfections, $-\delta_{top}(\theta)$ and $-\delta_{bot}(\theta)$, were applied as displacements to the upper and lower ends of the shell, respectively, at the beginning of the analysis to simulate a full contact condition between the shell ends and the loading platens. Then, the experimentally measured end-shortening displacement Δ and upper loading-platen rotations ϕ_y and ϕ_z were applied to the upper shell end while holding the lower shell end fixed as illustrated in Fig. 1.

Failure Analyses

A conventional Tsai-Wu tensor failure criterion was used to predict material failure in the shells. Two additional failure criteria were used and include a delamination failure criterion and an in-plane failure criterion. The transverse shear stresses were assumed to be distributed parabolically through the shell-wall thickness. The material allowable values used in the criteria are: longitudinal strength = 124.0 ksi, transverse

strength = 8.4 ksi, and shear strength = 11.6 ksi. When either failure criterion is equal to or greater than one, the material is assumed to have failed. Each stress component of the failure criteria is examined to determine the mode of failure. The failure criteria were used to indicate the possibility of material failure and to establish failure trends associated with the composite shells.

PARAMETER UNCERTAINTY CHARACTERIZATION

Several shell parameter values have a significant amount of uncertainty, and an attempt to characterize the effects of these uncertainties was made. The shell parameters with uncertainties considered include uncertainties in geometric imperfection measurements, lamina fiber volume fraction, fiber and matrix properties, applied end-load distribution, and boundary condition stiffnesses.

Imperfection measurement uncertainty is due to the accuracy tolerance of the coordinate measurement device used to measure the shell-wall geometry and end-surface imperfection, and this tolerance is equal to ± 0.0006 in. This tolerance corresponds to less than 0.01% uncertainty in the shell-wall imperfection measurement (e.g., Fig. 2). The measurement tolerance corresponds to a $\pm 3.0\%$ uncertainty in the thickness measurement (e.g., Fig. 3), and approximately $\pm 6\%$ uncertainty in the shell-end imperfection measurement (e.g., Fig. 4). The uncertainty in fiber and matrix properties and fiber volume fraction was based on published data contained in Volume 2 of the MIL 17 Handbook for composite materials and from the material manufacturer. The nominal fiber and matrix properties can vary $\pm 5\%$ and the nominal fiber volume fraction can vary $\pm 3\%$. The nominal fiber properties used in the present study are: longitudinal modulus = 31.19 Msi, transverse modulus = 3.49 Msi, shear modulus of 1.81 Msi, and Poisson's ratio = 0.27. The nominal matrix properties used are: Young's modulus = 0.53 Msi, shear modulus = 0.22 Msi, and Poisson's ratio = 0.35. The nominal fiber volume fraction is equal to 0.62.

The applied load distribution uncertainty is due to the shell end-surface imperfection uncertainty and the uncertainty in the orientation of the loading platen with respect to specimen shell-ends while the load is being applied during the test. Applied load distribution uncertainties are characterized indirectly by comparing the measured and predicted axial strains at selected points near the shell top and bottom loading surfaces. A correction to the applied displacement distribution was determined from the differences in the measured and predicted strains as follows. A user-written program external to the STAGS code was used to analyze the differences in the measured and predicted strains for a specified applied load value. This program used an iterative predictor-corrector method to determine a correction to the applied shell-end displacements. A new finite-element analysis was conducted with this displacement correction included in the model. This process was repeated iteratively until the difference in the predicted and measured strains reached a predetermined tolerance. A typical predicted displacement correction is presented in Ref. 3 and the amplitude of the displacement correction is on the order of ± 0.0005 in.

Boundary condition stiffness uncertainty is due to uncertainties in the potting material stiffness and in the integrity of the bond between the potting material and the shell wall. Visual inspection of the specimens before and after testing indicated that the potting material has a tendency to separate from the shell wall. This boundary condition stiffness uncertainty was not rigorously characterized. However, results from several numerical experiments indicate that variations in the boundary stiffness can have a significant effect on the displacement and strains near the shell ends, and can affect the character of the collapse response of the shells, e.g., Ref. 4. Therefore, it was arbitrarily assumed that the effective axial and radial boundary stiffnesses could vary $\pm 10\%$.

RESULTS AND DISCUSSION

Analytically predicted and experimentally measured results for the six graphite-epoxy shells considered in this study are presented in this section. The predicted results were obtained from finite-element models of geometrically perfect shells and shells that include initial geometric shell-wall imperfections, shell-wall thickness variations and thickness-adjusted lamina properties, local shell-wall lamina ply-gaps, boundary support conditions, and nonuniform loading effects. In addition, uncertainties in geometric and material properties, loading distribution, and boundary stiffnesses were included in the analyses. These results are presented to illustrate the overall behavior of compression-loaded graphite-epoxy shells and the effects of imperfections and parameter uncertainties on their response. First, results illustrating a typical nonlinear response of the quasi-isotropic 8-ply shell are presented. Then, comparisons between selected analytically predicted results and experimentally measured results for the 8-ply and 16-ply shells are presented. The results include predicted and measured load–end-shortening response curves, predicted prebuckling, buckling and postbuckling deformation response patterns, and predicted material failures.

Typical Nonlinear Response of an Imperfect Compression-loaded Cylindrical Shell

Results from a nonlinear analysis of the imperfect 8-ply $[45/0/90]_s$ shell C3 are presented in this section. The nonlinear analysis results are from a shell model that includes the effects of the measured initial shell-wall geometric and thickness imperfections, thickness-adjusted material properties, measured loading variations, and elastic radial support conditions. The predicted load-shortening response of shell C3 is shown in Fig. 5a. The axial load P and end-shortening Δ are normalized with respect to the linear bifurcation buckling load of the geometrically perfect nominal shell, $P_{bif} = 42.59$ kips, and the nominal shell-wall thickness, $t = 0.04$ in, respectively. The load–end-shortening curve indicates a linear prebuckling response. General instability occurs at a normalized axial load of $P/P_{bif} = 0.977$, marked by the letter A. The general instability response is followed by a sudden reduction in the axial load supported by the shell and is associated with the transient collapse response of the shell. The corresponding load-time history of the transient collapse response is shown in Fig. 5b. The load-time history curve has a sudden reduction in axial load until the collapse response attenuates and the axial load achieves a steady-state value. The kinetic energy in the shell obtains a maximum value during the transient collapse response, dissipates over time, and the shell reaches a stable postbuckling equilibrium state after approximately 0.007–0.008 seconds. The effective axial stiffness of the specimen is reduced in the postbuckling load range as indicated by the reduction in the slope of the load-shortening response curve.

The transient deformation responses for selected time steps during the transient collapse response of shell C3, indicated by the letters A through F in Figs. 5a and 5b, are presented in Fig. 6a through 6f, respectively. Just before buckling occurs, the shell wall deformations are characterized by several localized ellipse-like buckles as indicated in Fig. 6a. The localization in the deformation pattern is caused by the combination of a local geometric shell-wall imperfection that is in the form of a significant variation in the shell-wall mid-surface geometry, and the intersection of a helical ply-gap and a circumferentially aligned ply-gap in the shell at $x/L_T = 0.25$ and $\theta = 210^\circ$. The localized deformations occur in regions with destabilizing compressive axial and circumferential stresses. After approximately 0.0012 seconds have elapsed in the transient response, a single ellipse-like buckle has grown in amplitude and couples with the destabilizing stresses in the shell wall to cause the general instability and collapse of the shell. The magnitude of the shell-wall radial displacement varies between ± 0.5 times the shell-wall thickness. After additional time has elapsed, additional local buckles have formed around the circumference and along the length of the shell as indicated in Fig. 6c, and the normalized axial load has decreased from 0.974 to 0.759. The magnitude of the shell-

wall radial displacement varies between +2 to -4 times the shell-wall thickness. As the buckling process continues, the normalized axial load has decreased further to 0.554, and the deformation pattern in the shell wall continues to evolve and additional ellipse-like buckles have formed around the circumference of the shell as indicated in Fig. 6d. In addition, some of the buckles in the shell begin to coalesce into larger diamond-shaped buckles. The magnitude of the shell-wall radial displacement varies between +3 to -7 times the shell-wall thickness. After approximately 0.01 seconds have elapsed, the kinetic energy in the shell has dissipated to a negligible level indicating that the transient response has attenuated, and the shell has deformed into the stable postbuckling mode-shape indicated in Fig. 6e. As loading continues, the diamond-shaped buckles increase in size and the magnitude of the radial deformations of the buckles and the outer-surface ridges increase to between +4 and -9 times the shell-wall thickness as shown in Fig. 6f.

Predicted and Measured Response Comparisons

Selected results from nonlinear analyses of the six composite shells are compared to the experimentally measured results in this section. The nonlinear analysis results are for shell models that include the effects of the measured initial geometric and thickness imperfections, thickness-adjusted material property variations, measured loading variations, elastic radial support conditions, and selected specimen parameter uncertainties. The specimen parameter uncertainties considered include uncertainties in the imperfection measurement accuracy, fiber and matrix properties, fiber volume fraction, applied load, and boundary stiffness. Upper and lower response bounds were determined based upon the results of a traditional combinatorial analysis of the effects of the selected parameter uncertainties. Predicted and measured load–end-shortening response curves are presented in this section.

Eight-ply shells.- Three sets of analytically predicted and experimentally measured load–end-shortening response curves for the 8-ply shells C1, C2, and C3 are shown in Fig. 7. The axial load P is normalized by EA , where E is the effective axial stiffness of the shell and A is the nominal shell cross-sectional area. The end-shortening Δ is normalized by the nominal shell length $L = 16.0$ in. The solid and dashed lines in the figure represent experimentally measured and analytically predicted results, respectively. Each shell has two predicted response curves representing predicted upper and lower bounds to the response based on specimen parameter uncertainties, and the regions between the response bounds are shaded for clarity. The measured buckling load of each shell is marked by a filled circle and the ultimate failure load of each shell is marked with an X. In addition, each shell has one or more analytically predicted failure boundaries represented by the dark gray solid lines in the figure. Each failure boundary is labeled with the number 1, 2, or 3, which denote matrix failure initiation, fiber failure initiation, and delamination failure initiation, respectively. The measured results indicate that the prebuckling responses are linear up to the general instability load. General instability occurs at normalized loads of $P/EA = 0.00122$, 0.0044 , and 0.0022 for specimens C1, C2, and C3, respectively, and are 7.8, 13.7, and 17.6% lower than the predicted linear bifurcation buckling loads for the corresponding geometrically perfect, nominal shells, respectively. The general instability loads are followed by a sudden reduction in the axial load supported by the specimens, which is associated with the unstable transient collapse response of the specimens. During collapse, the specimens buckled into the classical diamond-shaped general instability mode-shape, and the collapse response was accompanied by an audible snapping sound. In addition, no significant visible failures were observed in the specimens as a result of the collapse response. The specimens achieved a stable postbuckling equilibrium state and had additional load carrying capacity in the postbuckling load range. Additional audible popping sounds were heard during the loading of the specimens in the postbuckling load range, which suggests that a progressive accumulation of material failures is occurring in the specimens. The accumulation of material failures continued until the ultimate failure

of the specimens occurred. The results in Fig. 7 indicate that, for the most part, the measured responses fall within the analytically predicted response bounds. In particular, the results indicate that the measured response curves tend to correlate with the mid-point between the upper and lower predicted response bounds. The predicted results indicate that, in most cases, material failure in the specimens is likely to occur at load levels near the general instability load and in the postbuckling load range. More specifically, matrix compression failure is predicted to occur in specimens C2 and C3 near the general instability point, followed by fiber compression failures and delamination type failures in the postbuckling load range. In contrast, the analytically results predict that matrix and fiber compression failures occur in specimen C1 in the postbuckling load range. These failure predictions correlate well with the failure trends observed in the tests. Predicted initial post-collapse radial displacement contours and the corresponding observed moiré fringe patterns for these specimens were observed to correlate well, as shown in Ref. 4.

Sixteen-ply shells.- Analytically predicted and experimentally measured load–end-shortening response curves for the 16-ply shells C4 through C6 are shown in Fig. 8. The axial load P is normalized by EA , where E is the effective axial stiffness of the shell and A is the nominal shell cross-sectional area. The end-shortening Δ is normalized by the nominal shell length $L = 16.0$ in. The solid and dashed lines in the figure represent experimentally measured and analytically predicted results, respectively. Each shell has two predicted response curves representing predicted upper and lower bounds to the response based on specimen parameter uncertainties, and the regions between the response bounds are shaded for clarity. The measured buckling load of each shell is marked by a filled circle and the ultimate failure load of each shell is marked with an X. In addition, each shell has one or more analytically predicted failure boundaries represented by the dark gray solid lines in the figure. Each failure boundary is labeled with the number 1, 2, or 3, which represent matrix failure initiation, fiber failure initiation, and delamination failure initiation, respectively. The measured results indicate that the initial load-shortening responses are, for the most part, linear up to the limit-point load for each specimen as indicated in the figure. However, the load-shortening responses for specimens C5 and C6 have a slight nonlinear behavior at end-shortening values greater than $\Delta/L = 0.004$. General instability occurs at normalized loads of $P/EA = 0.0027$, and 0.0049 for specimens C4, and C6, respectively, and are 16.8, and 18.4% lower than the predicted linear bifurcation buckling loads for the corresponding geometrically perfect, nominal shells, respectively. The results show that the general instability loads of specimens C4 and C6 coincide with the ultimate failure loads of the specimens, and these specimens do not have postbuckling load carrying capacity. More specifically, experimental results indicated that, upon collapse, specimens C4 and C6 have a significant amount of material failure including fiber and matrix compression failures and delamination failures, which caused the ultimate failure of the specimens. The predicted results indicate that, in most cases, the initiation of material failure is likely to occur during the initial portion of the transient collapse response as shown in Fig. 8, and these results explain the observed failure trends in specimens C4 and C6. In contrast, specimen C5 does not have a general instability load, rather, this specimen fails completely at a load of $P/EA = 0.0062$, which is 43.9% lower than the predicted linear bifurcation buckling load for the corresponding geometrically perfect, nominal shell. The overall failure of this specimen is characterized by a significant amount of delamination failures and fiber and matrix compression failures around the entire circumference of the shell. Post-test inspection indicated that the overall failure of the shell might have been initiated by a material failure near an axially aligned ply-gap in the shell wall. Predicted initial post-collapse radial displacement contours and the corresponding observed moiré fringe patterns for specimen C4 were observed to correlate well. Similar results were obtained for specimen C6 and indicate similar failure trends.

CONCLUDING REMARKS

The results of an experimental and analytical study of the effects of imperfections on the nonlinear response and buckling loads of unstiffened thin-walled compression-loaded graphite-epoxy cylindrical shells are presented. Numerical results for the nonlinear prebuckling, transient buckling, and postbuckling response of shells with measured imperfections are presented. The numerical results include the effects of traditional initial geometric shell-wall mid-surface imperfections and the effects of other nontraditional imperfections. These nontraditional imperfections include shell-wall thickness variations, material property variations, shell-end geometric imperfections, local shell-wall ply-gaps associated with the fabrication process, variations in loads applied to the end of the shell, and elastic boundary support conditions. In addition, upper and lower bounds to the nonlinear response of the shells are presented, which were determined from a combinatorial analysis of the effects of uncertainties in the values of several shell parameters. The uncertainties considered in the present study include uncertainties in the geometric imperfection measurements, lamina fiber volume fraction, lamina fiber and matrix properties, boundary condition stiffnesses, and applied load distribution. A high-fidelity nonlinear shell analysis procedure has been used to predict the nonlinear response and failure of the shells, and the analysis procedure accurately accounts for the effects of these traditional and nontraditional imperfections and parameter uncertainties on the nonlinear response and failure of the shells. The analysis results generally correlate well with the experimental results indicating that it is possible to predict accurately the complex nonlinear response and buckling loads for compression-loaded composite shell structures.

The numerical results indicate that the effects of the traditional and nontraditional imperfections, and uncertainties in the values of selected parameters considered in this study can be important for predicting the buckling loads of composite shells since they can significantly affect the nonlinear response and buckling loads of the shells. The results indicate that, for the most part, the measured response of the shells falls mid-way between the predicted upper and lower bounds to the response that are associated with the uncertainties or variations in the shell parameters considered in the study. These results indicate that the nonlinear analysis procedure used in this study can be used to determine accurate, high-fidelity design knockdown factors and response bounds that can be used for predicting composite shell buckling and failure loads in the design process. The traditional and nontraditional imperfections considered in this study could be used to formulate the basis for a generalized imperfection signature of a composite shell that includes the effects of variations or uncertainties in the shell-geometry, fabrication-process, load-distribution and boundary stiffness parameters. The high-fidelity nonlinear analysis procedure used in this study can be used to form the basis for a shell analysis and design approach that includes this generalized imperfection signature and addresses some of the critical shell-buckling design criteria and design considerations for composite shell structures. This high-fidelity nonlinear analysis procedure could be used in the shell design process without resorting to the traditional empirical shell design approach that can affect the cost of developing new composite shell designs.

REFERENCES

1. Anon., Buckling of Thin-Walled Circular Cylinders. NASA Space Vehicle Design Criteria, NASA SP-8007, September 1965.
2. Koiter, W. T., "On the Stability of Elastic Equilibrium," (in Dutch), H. J. Paris, Amsterdam, Holland, 1945; translation available as AFFDL-TR-70-25, February 1970, Wright-Patterson Air Force Base.

3. Hilburger, M. W., and Starnes, J. H., Jr., "High-fidelity Analysis of Compression-loaded Composite Shells," Proceedings of the 42nd AIAA/ASME/ASCE/AHS/ASC Structures, Structural Dynamics, and Materials Conference, Seattle, WA, 2001. AIAA Paper No. 2001-1394, April 2001.
4. Hilburger, M. W., and Starnes, J. H., Jr., "Effects of Imperfections on the Buckling Response of Compression-Loaded Composite Shells." *International Journal of Non-Linear Mechanics*, Vol. 37, 2000, pp. 623-643.
5. Rankin, C. C., Brogan, F. A., Loden, W. A., and Cabiness, H. D., "STAGS Users Manual, Version 3.0," Lockheed Martin Missiles & Space Co., Inc., Advanced Technology Center, Palo Alto, CA, Report LMSC P032594, 1999.

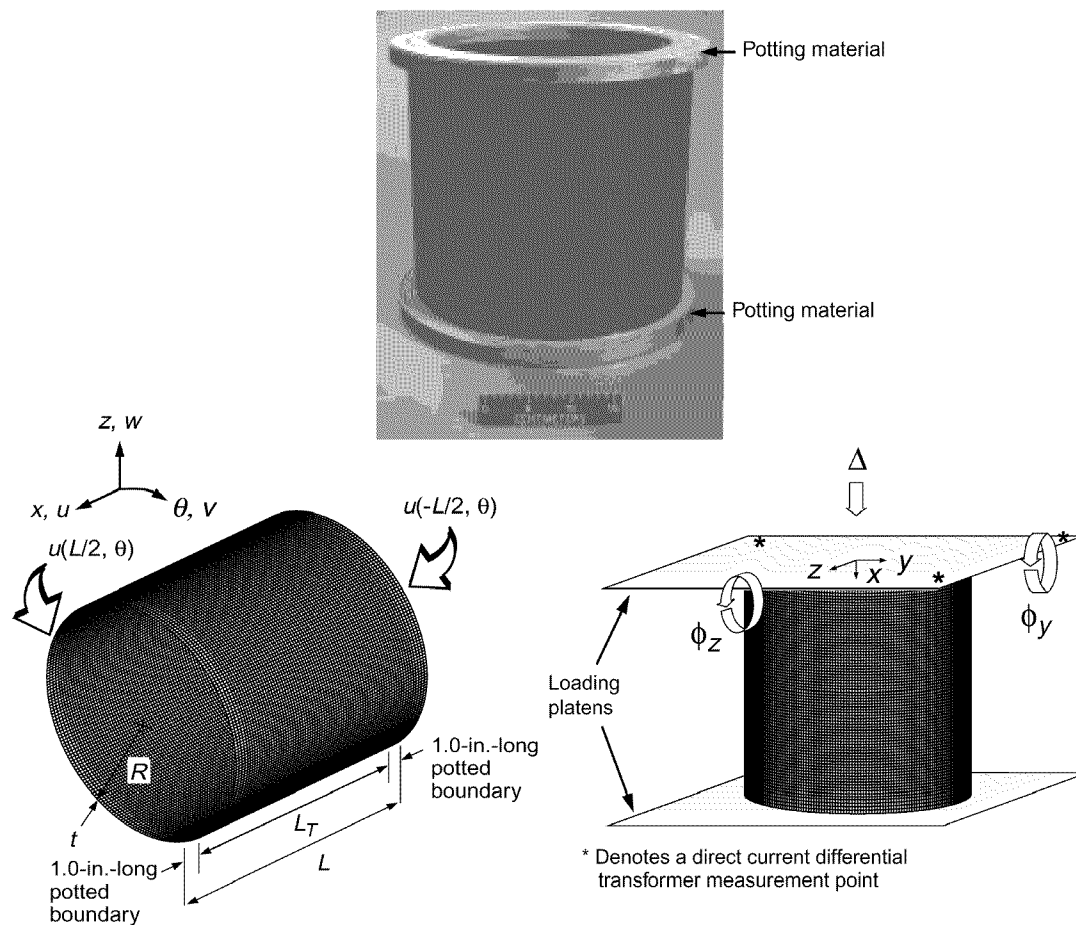


Fig. 1 Typical specimen, finite-element model geometry and loading conditions.

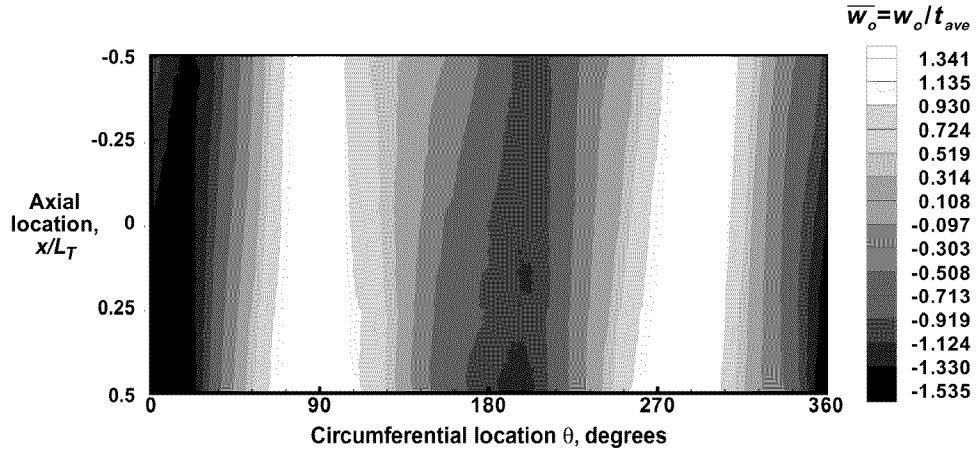


Fig. 2 Typical measured inner-surface imperfection shape for shell specimen C3.

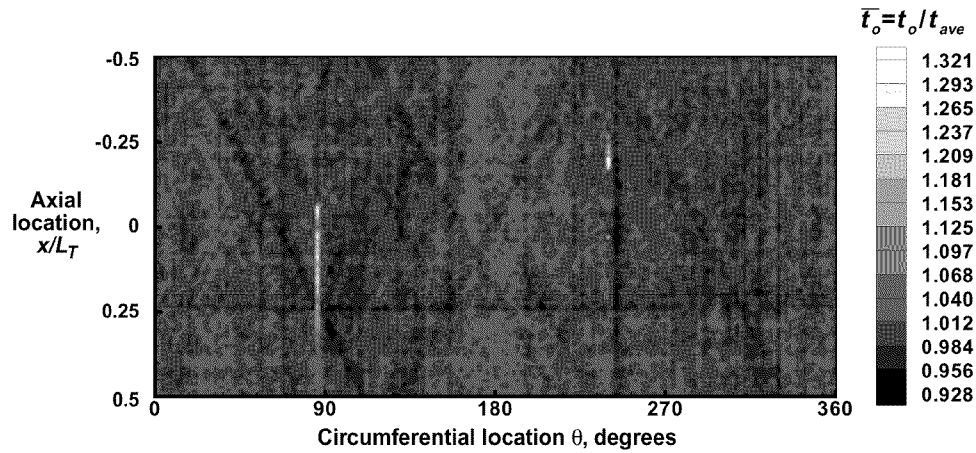


Fig. 3 Typical measured wall thickness variation for a shell specimen C3.

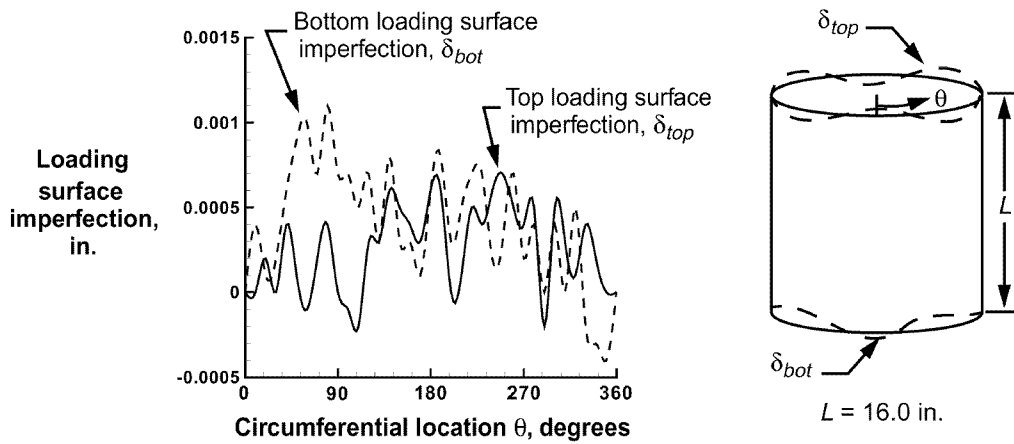


Fig. 4 Typical measured shell-end or loading-surface imperfections for a shell specimen C3.

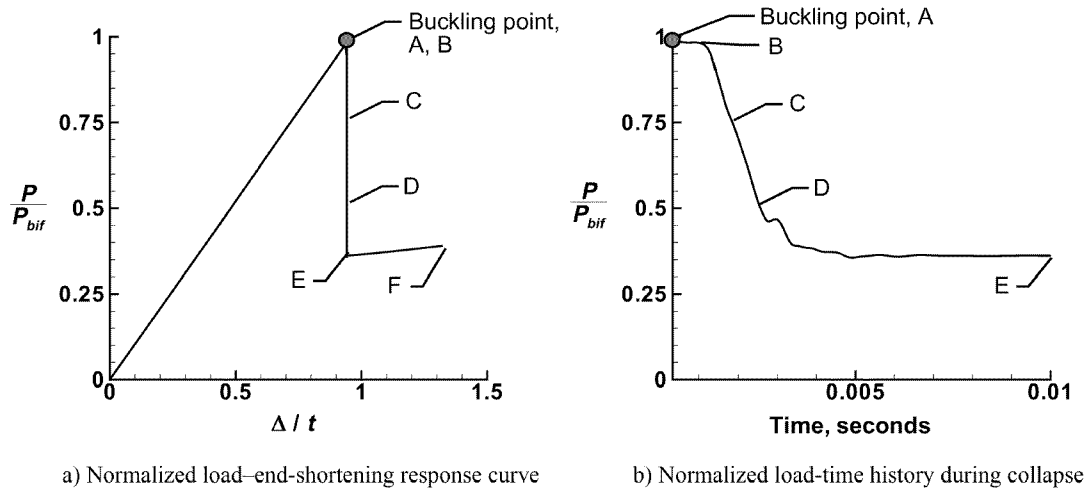


Fig. 5 Analytically predicted nonlinear response of an imperfect, compression-loaded, quasi-isotropic shell C3.

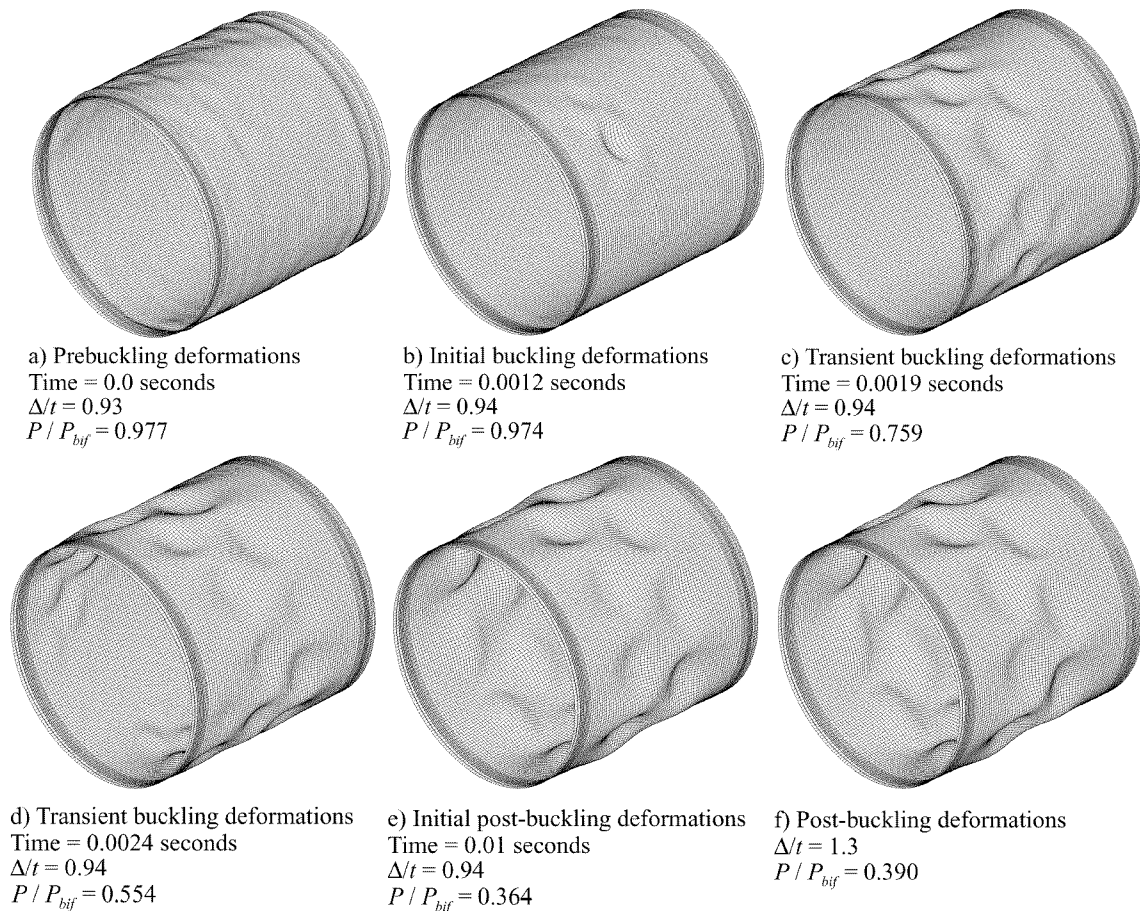


Fig. 6 Analytically predicted prebuckling, buckling, and postbuckling response of an imperfect, compression-loaded, quasi-isotropic shell C3.

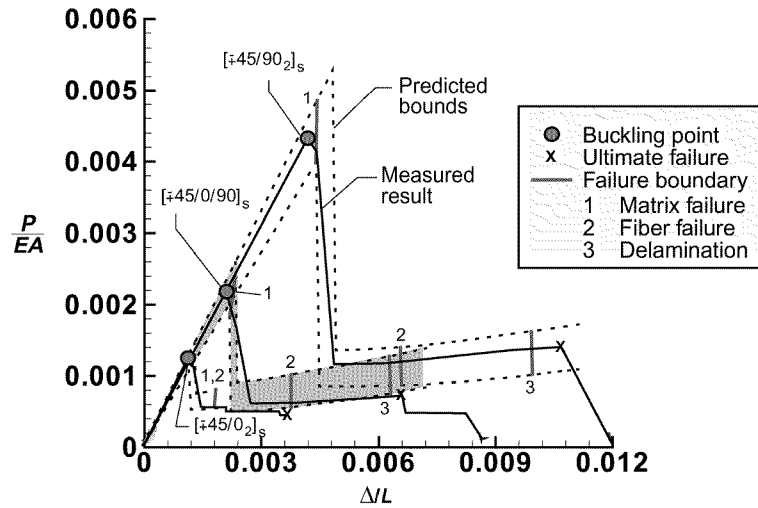


Fig. 7 Analytically predicted and experimentally measured load–end-shortening response curves for 8-ply compression-loaded shells; predicted results represent response bounds.

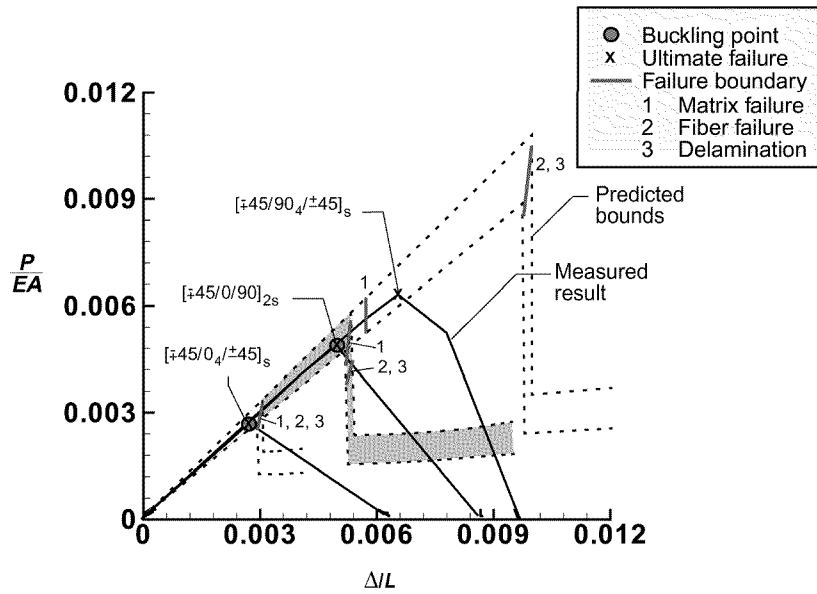


Fig. 8 Analytically predicted and experimentally measured load–end-shortening response curves for 16-ply compression-loaded shells; predicted results represent response bounds.